Redox behavior of tin in aluminosilicate melts: Implications for the fining process

Adrien Donatini, Peggy Georges, Tiphaine Fevre, Laurent Cormier, Daniel R Neuville

To cite this version:

Adrien Donatini, Peggy Georges, Tiphaine Fevre, Laurent Cormier, Daniel R Neuville. Redox behavior of tin in aluminosilicate melts: Implications for the fining process. International Journal of Applied Glass Science, 2025, pp.e70006. ⟨10.1111/ijag.70006⟩. ⟨hal-05248720⟩

Received: 21 May 2025 | Revised: 15 July 2025 | Accepted: 15 August 2025

DOI: 10.1111/ijag.70006

INTERNATIONAL JOURNAL OF
Applied Glass
SCIENCE

RESEARCH ARTICLE

Redox behavior of tin in aluminosilicate melts: Implications for the fining process

Adrien Donatini[1,2,3] | **Peggy Georges**[1] | **Tiphaine Fevre**[1] | **Laurent Cormier**[2] | **Daniel R. Neuville**[3]

[1]Corning European Technology Center, Avon, France

[2]Sorbonne Université, Muséum National d'Histoire Naturelle, UMR CNRS 7590, Institut de Minéralogie, Paris, France

[3]Géomatériaux, CNRS-IPGP, Université de Paris, Paris, France

Correspondence
Daniel R. Neuville, Géomatériaux, CNRS-IPGP, Université de Paris, 75005 Paris, France.
Email: neuville@ipgp.fr

Funding information
Association Nationale de la Recherche et de la Technologie, Grant/Award Number: 2021/0986

Abstract

Aluminosilicate glasses are widely used in everyday applications and can be seen as building blocks of modern technology, from display screens to glass-ceramics. However, due to their high viscosities, gas bubbles can only be removed from aluminosilicate melts at high temperatures, leading to significant energy costs. This fining process can be improved with the use of multivalent oxides such as SnO_2. In this study, extended x-ray absorption fine structure (EXAFS) and Raman spectroscopy were used to determine the local environment surrounding Sn(II) and Sn(IV) ions in a sodium aluminosilicate glass. In situ XANES spectroscopy enabled the quantification of Sn redox state at high temperature, allowing for the determination of thermodynamic parameters governing the Sn reduction. Our results show that Sn(IV) is octahedrally coordinated and linked to network-forming tetrahedra through corner-sharing, whereas Sn(II) is in a lower coordination number. Comparing the modeled behavior of Sn with that of Fe and Ce, it appears that SnO_2 is a suitable fining agent for aluminosilicate glasses as it undergoes reduction when the viscosity is sufficiently low for bubbles to escape the melt. Conversely, the use of CeO_2 leads to substantial gas release at higher viscosities, resulting in foam formation within the glass.

KEYWORDS
aluminosilicates, chemical fining, in situ measurements, Raman, Redox, XANES

1 | INTRODUCTION

Aluminosilicate and boro-aluminosilicate glasses are a widespread material family that covers multiple applications from everyday display glass[1,2] to vaccine vials[3] and reinforcement fibers.[4,5] In addition to their industrial relevance, aluminosilicates are of great interest in Earth sciences, as they are chemically close to mantle compositions.[6,7] From an industrial perspective, the interest and use of aluminosilicate glass stem from its outstanding mechanical properties.[8–10] These properties can be enhanced through ion exchange[11,12] or by incorporating elements such as lanthanides.[8] Lithium aluminosilicate melts are also common precursors for glass-ceramics, with applications ranging from cooktop induction plates[13,14] to energy storage systems due to high Li mobility.[15]

The main drawback of aluminosilicate and boro-aluminosilicate glasses is their high viscosity. As the aluminum content increases, the melt viscosity rises accordingly, reaching a maximum near the tectosilicate join.[4] This high viscosity drives the processing temperatures up, especially during melting. For example, boro-aluminosilicate E-glass fibers are processed at temperatures up to 1500°C,[16] while LCD panels require temperatures as high as 1600°C.[17] Reaching such high temperatures requires substantial energy, which represents a major cost for the aluminosilicate glass making compared to traditional window glass manufacturing. This is especially true for the fining step that requires the highest temperatures. During fining, gas bubbles that come from raw materials or are trapped between grains must escape from the melt to ensure a clear, bubble-free, high-quality final product. Increasing the temperature lowers the melt viscosity, facilitating bubble removal. The efficiency of the fining step can be measured by the number of remaining bubbles after processing.[18,19] The goal is to remove all bubbles at the lowest temperature possible, in the shortest amount of time.

To enhance fining efficiency, several methods can be used, such as the bubbling of gas[20] or the addition of fining agents to the raw materials. These agents include sulfates,[21] nitrates,[22] or multivalent oxides[17,23,24]; As_2O_5, Sb_2O_3, SnO_2, and CeO_2 are multivalent oxides that are commonly used as fining agents. During glass melting, as the temperature increases, these oxides dissolve in the melt and undergo partial reduction. Upon their reduction, they release oxygen gas, which increases the size of existing bubbles and enhances their escape from the melt.[25] Consequently, the fining capability of these oxides is strongly tied to their ability to be reduced upon heating, which depends on their redox behavior. However, the redox equilibrium of multivalent elements is influenced by various parameters, such as temperature, oxygen fugacity, and melt composition.[26–28] The relationship between the reduction of multivalent elements and the amount of gaseous oxygen release is complex and often requires an understanding of the local structure and coordination of these elements.[29,30] Moreover, the redox state at room temperature is not always representative of the redox state in the molten state,[31] making room temperature analyses insufficient when assessing the high-temperature redox state.

In this study, we used extended x-ray absorption fine structure (EXAFS) and Raman spectroscopy to investigate the local structure of Sn ions in a sodium aluminosilicate glass. In situ XANES was used to monitor the evolution of Sn redox state as a function of temperature. These measurements allowed for a thermodynamic parametrization of Sn redox behavior in sodium aluminosilicate glass. The Sn behavior was then compared to that of Ce and Fe in the same glass, to differentiate the fining abilities of these three multivalent elements.

TABLE 1 Compositions (wt%) measured by EPMA.

Sample	SiO_2	Al_2O_3	Na_2O	FeO[a]	SnO_2[b]
NAS0	61.9 ± 0.8	19.2 ± 0.3	18.1 ± 0.3	<0.005	0
NASS0_1	62.4 ± 0.8	18.8 ± 0.2	18.0 ± 0.2	0.012	0.18 ± 0.01
NASS0_10	60.3 ± 0.7	18,6 ± 0.2	17.3 ± 0.2	0.008	2.22 ± 0.09
NASS0_20	59.6 ± 0.9	19.5 ± 0.3	17.6 ± 0.2	0.042	2.60 ± 0.04

[a] Total iron given as FeO.

[b] Total tin given as SnO_2.

2 | EXPERIMENTAL SECTION

2.1 | Glass synthesis

The base undoped glass used in this study, $68.2SiO_2$–$12.5Al_2O_3$–$19.3Na_2O$ (mol%), is the same as that in a previous investigation.[32] The obtained glass was finely ground in an agate mortar and mixed with SnO_2 (99.7%, Corning) to achieve molar concentrations of SnO_2 ranging from 0.1 to 2 mol% of SnO_2. The samples were labeled NASS0_*x*, with *x* corresponding to the molar concentration of SnO_2 in per thousand (‰) with respect to previous studies. The mixture was then melted four times, each for 2 h at 1600°C in a Pt crucible. The liquids were quenched by dipping the bottom of the crucible into water. Sample homogeneity was checked by performing three Raman spectra in different regions of the sample.

2.2 | EPMA

Electron probe micro-analysis (EPMA) measurements were performed on a Cameca SX-Five at the Camparis facility (Sorbonne Université, Paris). A voltage of 25 kV and a beam size of 20 µm were used for all measurements. For Si, Na, and Al, a current intensity of 4 nA and a counting time of 10 s were used, while a current intensity of 200 nA and a counting time of 20 s were applied to measure the low concentrations of Fe. The standards used for calibration were Albite ($NaAlSi_3O_8$) for Na and Si, $(Mg,Fe)_3Al_2(SiO_4)_3$ for Al, FeS_2 for Fe, and Cassiterite (SnO_2) for Sn. At least 10 measurements were performed for each composition, with the average value reported in Table 1.

2.3 | x-Ray absorption spectroscopy at Sn K-edge

Sn K-edge XAS spectra were recorded on the SAMBA beamline located at the SOLEIL synchrotron facility (Saint-Aubin, France). During the measurements, SOLEIL operated at 2.75 GeV and 500 mA. For room temperature spectra, glass slices were polished to the appropriate thickness for measurements. A double crystal monochromator equipped with two Si(220) crystals was used to tune the energy. Energy was calibrated using a tin foil. Data were collected in fluorescence mode using a 35-element monolithic planar Ge detector (Canberra). The beam size was 200 by 300 μm^2. Room temperature EXAFS data were collected from 29 to 30.2 keV, with a 0.5 eV step. The x-ray absorption near-edge structure (XANES) data were collected between 29 and 29.2 keV with a 0.5 eV step, from 29.2 to 29.4 keV with a 0.2 eV step, and from 29.4 to 29.8 keV with a 0.5 eV step. High-temperature experiments were conducted by loading glass powder into a 500 μm hole of a 90Pt-10Ir wire.[33] The wires were heated by passing an electric current through them. Each wire was calibrated using the procedure detailed by Neuville and Mysen.[34] The temperature measurement error was conservatively set to ±20°C. All XAS spectra were processed using the Larch software.[35]

2.4 | Raman spectroscopy

Unpolarized Raman spectra were acquired using a Labram HR Evolution spectrometer equipped with a Peltier-cooled CCD and an 1800 lines per mm grating. The samples were excited with a Coherent MX 488 nm solid-state laser focused through a ×50 Olympus objective (LMplanFl, WD: 10.6 mm) on the sample surface. The spectral resolution of the setup is approximately 1.7 cm^{-1}, and the spatial resolution is approximately 1 μm. The laser power at the exit was adjusted to 600 mW. Spectra were acquired from 20 to 1500 cm^{-1} thanks to an ultralow frequency (ULF) filter to attenuate the laser signal. A linear baseline was fitted and removed over the 1350–1500 cm^{-1} range. Spectra fitting was performed using the Fityk software.[36]

3 | RESULTS

3.1 | Sample synthesis and SnO_2 volatilization

Analyzed chemical composition of the glasses is analyzed and given in Table 1.

The amount of SnO_2 measured by EMPA for samples NASS0_1 and NASS0_10 is in good agreement with the nominal values. However, the measured concentration of SnO_2 in NASS0_20 is significantly lower than the expected value (of about 4.4 wt%). Additional EPMA measurements on this sample revealed a gradient in SnO_2 contents, with all concentrations being lower than the nominal value. This shows that the tin content in the NASS0_20 sample is heterogeneous. A possible explanation for this behavior is the volatilization of Sn during sample elaboration, which occurs when exposed to air for more than 8 h. Indeed, Sn is considered a moderately volatile element in the Earth science literature.[37] Recent thermodynamic calculations considering trace amounts of Sn showed that about 8% of Sn was in vapor form at equilibrium for a granodiorite composition (about 66 mol% SiO_2).[38] Given that the crucible was left open in the furnace, this volatilization behavior is likely more pronounced than the calculations suggest. Moreover, Sn cannot be considered as a trace element in NASS0_20, and Henry's Law used in the thermodynamic calculations may not apply to our samples. This could increase the volatility of Sn at higher concentrations and explain why NASS0_1 and NASS0_10 seem less affected by this behavior. Another possible explanation might be the limited solubility of Sn in our system, causing the "excess" Sn to volatilize. However, more investigation is required to better understand SnO_2 incorporation in aluminosilicate systems.

Fe was not added intentionally to the glass. Its presence can be explained by impurities in the raw materials (SiO_2) as well as potential cross-contamination via the crucibles, as Fe-rich compositions were also synthesized for other projects. However, the Fe concentration is always much lower than that of Sn (by at least a factor of 15). Therefore, the presence of Fe in such low concentrations will not affect Sn redox state.[31]

3.2 | XANES spectroscopy at Sn K-edge

The XANES spectra at Sn K-edge (Figure 1) can be described as the sum of two contributions, the first one being the main feature at 29 210.5 eV, followed by a shoulder at 29 228 eV. These two features are present in the spectra of both the SnO and SnO_2 references as well as in the glass sample.

The position of the absorption edge is at lower energies for the Sn(II) reference compared to the Sn(IV) reference (29 198.8 eV vs. 29 201.8 eV). Although these values differ slightly from those reported by Farges et al.,[39] the energy difference between the Sn(II) and Sn(IV) edges is consistent with their study. The absolute difference (of about 2.4 eV) can be attributed to the calibration difference between Farges et al.'s study and ours. The edge in the NASS0_1 spectrum lies between those of SnO and SnO_2, showing that both Sn(II) and Sn(IV) are present in the glass. The method used to quantify the redox state is the "half-step" method described by Farges et al.[39] The energy at the halfway point of the absorption edge is measured and compared to that of crystalline references. In the

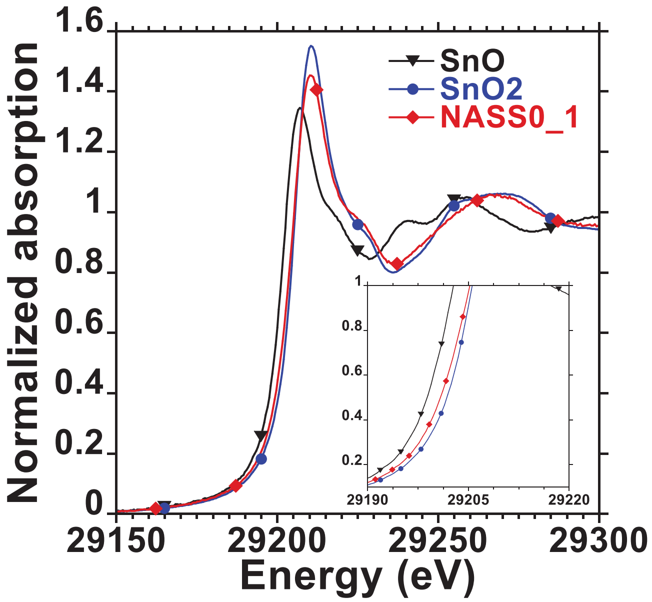

FIGURE 1 Room temperature XANES spectra at the Sn K-edge for crystalline references and the sample NASS0_1.

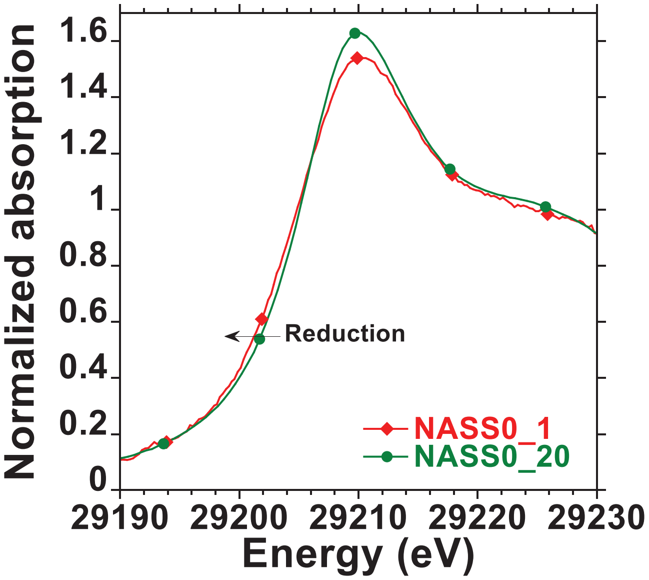

FIGURE 2 Room temperature XANES spectra at the Sn K-edge for NASS0_1 and NASS0_20.

spectrum of NASS0_1 (Figure 1), the half-step point is located at 29 200.8 eV. Using a linear combination of the two references, the redox ratio is quantified at 32% ± 8% Sn(II). The precision of this method is limited by the experimental resolution and the signal/noise ratio of the measurements.

No photoionization was observed at room temperature for measurements performed on NASS0_10 and NASS0_20. Mild photoreduction was observed in NASS0_1 for long exposure times (~8% difference after 10 scans). Although this effect was minor, the data presented here for NASS0_1 are for the first spectrum acquired.

4 | DISCUSSION

4.1 | Influence of total Sn concentration on Sn redox state at room temperature

The XANES spectra of NASS0_1 and NASS0_20 are different, as shown in Figure 2. It is important to note that those two samples underwent identical synthesis procedures at 1600°C. The half-step is at lower energies for NASS0_1 than it is for NASS0_20, and the intensity of the white line at 29 210.5 eV is also lower in the spectrum of NASS0_1. These observations indicate qualitatively that Sn is more reduced in NASS0_1 than in NASS0_20. Using the half-step method, we can quantify the redox state of Sn at different concentrations (Table 2).

Sn is quantifiably more reduced in NASS0_1 than in NASS0_20. Due to the high uncertainty inherent to the half-step method, the difference between NASS0_10 and NASS0_20 is less clear. This is coherent with the measured concentrations shown in Table 1, where we show that the concentration of Sn in NASS0_10 and NASS0_20 is very similar. However, it appears that Sn is more reduced at lower concentrations. A similar behavior has already been observed in the case of Fe.[40] This phenomenon can be linked to the activity coefficients of the different Sn species. This relationship can be seen through Equation (1).

TABLE 2 Redox state of Sn at room temperature.

Sample	Half-step (eV)[a]	% [Sn(II)] (±8)
Sn(II)O	29 198.8	100
NASS0_1	29 200.8	32
NASS0_10	29 201.4	14
NASS0_20	29 201.6	7
Sn(IV)O	29 201.8	0

Note: Error bars are calculated from the energy resolution.
[a] See Section 3.2 for the method.

$$Sn^{2+}_{melt} + \frac{1}{2}O_{2(g)} \rightleftharpoons Sn^{4+}_{melt} + O^{2-}_{melt} \tag{1}$$

The associated equilibrium constant is:

$$K_1 = \frac{a_{Sn^{4+}_{melt}} * a_{O^{2-}}}{a_{Sn^{2+}_{melt}} * \sqrt{f_{O_2}}} \tag{2}$$

with $a_{Sn^{4+}_{melt}}$ being the activity of the corresponding species and f_{O_2} the oxygen fugacity. By introducing the fraction of reduced species x_{red}, the activity coefficients γ and the total Sn concentration $[\mathrm{Sn}]_{\mathrm{tot}}$, these equilibrium constants can be rewritten as follows:

$$K_1 = \frac{(1 - x_{\mathrm{red}}) * [\mathrm{Sn}]_{\mathrm{tot}}}{x_{\mathrm{red}} * [\mathrm{Sn}]_{\mathrm{tot}}} * \frac{\gamma_{\mathrm{Sn}^{4+}} * a_{\mathrm{O}^{2-}}}{\gamma_{\mathrm{Sn}^{2+}} * \sqrt{f_{\mathrm{O}_2}}} \tag{3}$$

Even though the $[\mathrm{Sn}]_{\mathrm{tot}}$ simplify themselves in K_1, the activity coefficients of Sn(II) and Sn(IV) are sensitive to the total Sn concentration. At lower concentrations, like in the NASS0_1 sample, Henry's Law applies, meaning that the activity coefficients of Sn(II) and Sn(IV) are both equal to 1. However, the activity coefficients of oxides in silicate melts do not follow a linear trend with concentration, but rather exhibit a log-linear form.[41] The deviation to linearity depends on the role of the oxide; it has been shown that the activity coefficient of network modifiers exhibits a more pronounced deviation from ideality than for network formers.[41] For Sn, Sn(IV) and Sn(II) play two different structural roles in silicate glasses.[42] Therefore, it is safe to assume that the activity coefficients of Sn(II) and Sn(IV) will not follow the same trend with increasing concentration. This deviation is absent or negligible at low concentrations where Henry's Law applies. However, at higher concentrations, the activity of Sn(II) and Sn(IV) is most likely different, which can influence the redox state in various ways. This behavior has been evidenced in the case of Fe, for instance[43] and can explain why the redox state of Sn is more oxidized in NASS0_20 sample than in NASS0_1. This result shows the importance of considering the total Sn concentration when predicting its redox state.

4.2 | Local structure of Sn in aluminosilicate glass

EXAFS spectroscopy allows for the determination of the local environment around Sn. The Fourier transform of the EXAFS signal, $\chi(k)$, for NASS0_20 shows a first contribution at $R = 1.5$ Å (uncorrected phase-shift position), which corresponds to the [Sn]–O–[Sn] backscattering path (Figure 3B). It is important to note that this does not correspond to the real Sn–O distance but rather an apparent one. This contribution is also found in the Fourier transform of SnO_2, indicating qualitatively that the first coordination sphere of Sn in aluminosilicate glass is similar to the one in SnO_2. The [Sn]–O–[Sn] path in SnO is found at much higher R, which does not align with the glass data. Regarding the second coordination sphere, the [Sn]–Sn–[Sn] path in SnO and SnO_2 is found at R values higher than 3 Å. However, no such contribution is visible on the Fourier transform of the NASS0_20 sample. This suggests that the second coordination sphere of Sn in NASS0_20 glass does not involve another Sn ion. We can conclude that even at relatively high Sn concentrations, no detectable clustering occurs in this system. This observation also confirms the absence of significant SnO_2 crystallization in the glass.

The second coordination sphere is due to cationic species, which can either be network modifiers or formers. To accurately identify the different coordination spheres around Sn, the EXAFS spectrum in Figure 3A was fitted using backscattering pathways reported by Uchida et al.[44] for eakerite ($SnCa_2Al_2Si_6O_{16}(OH)_6$). We used eakerite as it possesses both [Sn]–O–[Sn] and [Sn]–Si–[Sn] backscattering pathways, which are plausible in our glasses. For details on the FEFF program used for the fitting process, readers are referred to page 65 of Newville.[45]

The $\chi(k)$ signals were fitted in the 1–3.5 Å range in R-space, considering only the first two coordination shells. The fits deviate from experimental data for $k < 4$ Å^{-1}, which may indicate multiple scattering behaviors at low k. The coordination number, CN, for Sn in NASS0_20 is the same as for SnO_2. This confirms previous studies, indicating that Sn(IV) is present as $SnO_6{}^{8-}$ units in silicate glasses.[39,46] The Sn–O distance in NASS0_20 is consistent with that found in cassiterite or eakerite.[47] This similar local structure may explain the tendency of Sn(IV) to crystallize. Although the error bars overlap, the data suggest that the CN of Sn differs between NASS0_1 and NASS0_20 (Table 3). While this difference could be due to concentration effects alone, the most probable explanation is the variation in Sn redox state between the two samples. Indeed, Sn is nearly fully oxidized in NASS0_20, whereas it is significantly reduced in NASS0_1. This suggests that Sn(II) has a lower CN than Sn(IV), consistent with the conclusions of McKeown et al.[46] who reported that dilute Sn is present as a mixture of 60% $\mathrm{Sn(IV)O_6}{}^{8-}$ and 40% $\mathrm{Sn(II)O_4}{}^{6-}$. This redox ratio is similar to that found in NASS0_1. The reduction reaction of Sn can be expressed as:

$$\mathrm{Sn\,(IV)\,O_6^{8-}} \rightleftharpoons \mathrm{Sn\,(II)\,O_4^{6-}} + \mathrm{O^{2-}} + \frac{1}{2}\mathrm{O_{2(g)}} \tag{4}$$

This reaction indicates that oxygen gas is released during Sn reduction. This oxygen release plays a crucial role in the fining process, which will be discussed in Section 4.4.

The second coordination sphere around Sn in NASS0_20 was fitted using the [Sn]–Si–[Sn] path in eakerite. The resulting fit is convincing with the Sn–Si distance very close to that in eakerite (3.33 Å).[47] In this mineral, Sn resides in an octahedral site sharing corners with SiO_4 tetrahedra. Given the similarity in Sn–Si distances in NASS0_20, it is reasonable to assume that Sn occupies a similar local environment in aluminosilicate glasses. Although the fitting was performed using a [Sn]–Si–[Sn] path, a similar result is obtained when considering a [Sn]–Al–[Sn] path, as Si and Al are challenging to

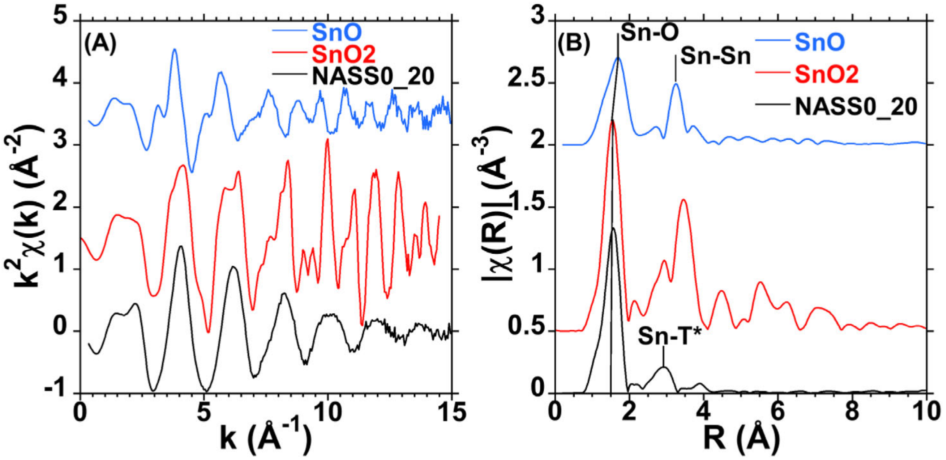

FIGURE 3 (A) Weighted-EXAFS (extended x-ray absorption fine structure) signal of the crystalline references and the NASS0_20 glass. (B) Corresponding Fourier transform of the EXAFS signal.

TABLE 3 Fitting results for the standard and the glass.

Sample	Neighbor	CN	*R* (Å)	σ^2 (Å^2)	Reduced χ^2	%Sn(II)
SnO	O	4.0 ± 0.4	2.20 ± 0.01	0.007 ± 0.001	24.04	100
SnO_2	O	5.8 ± 0.6	2.04 ± 0.01	0.003 ± 0.001	2.34	0
NASS0_1	O	5.1 ± 0.4	2.04 ± 0.01	0.003 ± 0.001	1.86	32 (±8%)
	Si[a]	2 ± 1	3.30 ± 0.02	0.007 ± 0.006		
NASS0_20	O	5.8 ± 0.4	2.04 ± 0.01	0.003 ± 0.001	1.57	7 (±8%)
	Si[a]	2.3 ± 0.9	3.32 ±0.01	0.004 ± 0.003		

Note: Only the first coordination sphere is presented for the standards. The uncertainty on the last digit is given in brackets. CN, *R*, and σ are the coordination number, average distance, and Debye–Waller factor determined in the fitting process. The %Sn(II) is determined by XANES analysis. All fits were performed with $S_0^2 = 0.94$.

[a] The second shell was fitted using Sn–Si paths, but it is not possible to distinguish Si and Al in the EXAFS signal due to their similar scattering properties.

distinguish in EXAFS. For this reason, the second shell contribution in Figure 3B is labeled Sn–T, reflecting the possible presence of both Si and Al (see Figure 4 for the fitting of the EXAFS data).

The interpretation of the Raman spectra of the undoped NAS0 glass was previously discussed.[32] Upon Sn addition, the Raman spectra change in two different regions, which are highlighted in the difference spectra in Figure 5B. As shown in Table 2, Sn is fully or almost fully oxidized in NASS0_20. Therefore, any differences between the Raman spectra of NASS0_20 and NAS0 can be attributed to the introduction of Sn(IV) in the glass. Though it is possible that a change in Sn redox state would affect the Raman spectra, as is the case for Ce redox state,[48] our results do not allow us to discuss that. A decrease in intensity occurs around 1100 cm^{-1}, as well as a shift of the maximum toward lower energies. This region holds information on the network polymerization and, more specifically, on the relative proportions of the Q^n species.[32,49] A shift of this band to lower wavenumbers is associated with a change from Q^n units to Q^{n-1} units. The changes observed in this region can be explained as a decrease in Q^3 population and a rise in Q^2 species. Therefore, these spectral changes could indicate a depolymerization of the silicate network upon Sn addition, though the extent of this effect is difficult to quantify with Raman spectroscopy.

Upon Sn(IV) addition, a new contribution appears in the 500–600 cm^{-1} range. Contributions in this range are typically attributed to rings in the silicate structure.[49,50] Therefore, the increase at 540 cm^{-1} could be interpreted as a change in the proportion of rings upon Sn(IV) addition. However, the preferred hypothesis is that this contribution arises from the SnO_6 octahedra connected to the TO_4 tetrahedra, evidenced by EXAFS spectroscopy. Indeed, this structural arrangement is also found in eakerite and malayaite, the Raman spectra of which have their most intense contribution in the 500–600 cm^{-1} range.[51]

4.3 | In situ Sn redox state and thermodynamic modelling

Although the determination of Sn redox state at room temperature is important, it is also necessary to monitor its temperature dependence to fully understand its role as a fining agent. Samples were equilibrated in a 90Pt-10Ir wire

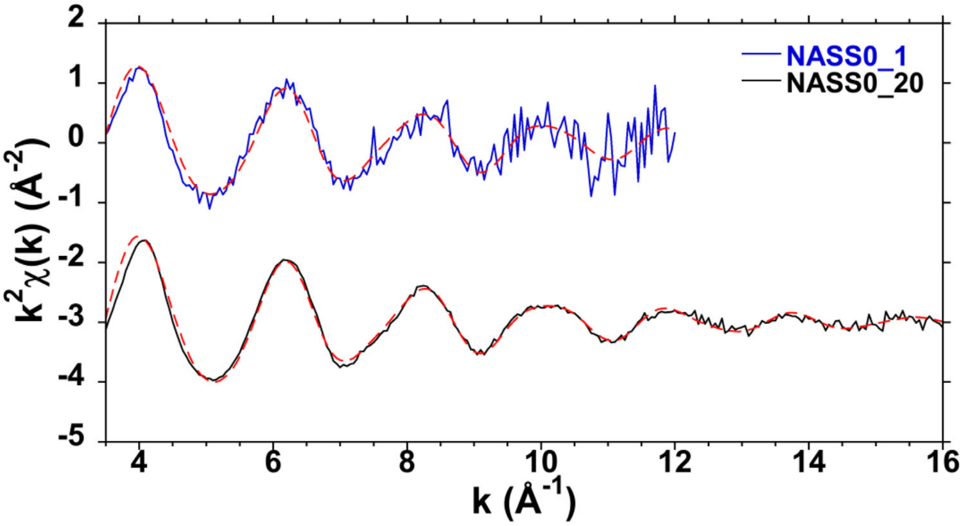

FIGURE 4 Weighted-EXAFS (extended x-ray absorption fine structure) spectra fitting of Sn-containing aluminosilicate glasses. The fits obtained are the dashed red curves.

microfurnace until no variation was observed. This equilibration time varied between 2 h at 1000°C to less than 5 min above 1500°C.

When the sample is equilibrated at 1300°C for 90 min, the edge position at the half-step point is the same as in the SnO_2 reference (Figure 6A). We can conclude that Sn is fully oxidized in the glass at 1300°C. It is important to note that the white line intensity decreases at higher temperatures, which does not appear to be linked to a reduction of Sn, as the edge energy still shows complete oxidation of Sn. Figure S1 shows Sn K-edge spectra recorded at different temperatures, highlighting the decrease in the white line intensity with increasing temperature. A possible explanation is a change in the edge structure due to thermal and disorder effects, as evidenced for lighter elements such as Al or Si.[52] Indeed, an increase in temperature can favor hybridization of orbitals, resulting in a change in the XANES contribution relative intensity. Another possibility is a change in Sn coordination state from the glassy to the molten state, as mentioned in previous studies.[46,53] However, the data presented here do not allow us to further discuss a change in Sn's local environment. Most importantly, the changes in the white line intensity do not affect the determination of the redox state through the half-step method, as the edge does not shift in energy.

For the NASS0_1 composition, when the temperature is increased to 1610°C, the edge of the XANES spectrum shifts to lower energies, which indicates Sn reduction. The edge position of NASS0_1 measured at room temperature after quenching is very close to the value measured in situ at equilibrium at 1610°C. This shows that the high-temperature redox state of Sn is frozen upon quenching, resulting in the observed room temperature redox state. A similar behavior was shown in Ce- and Fe-bearing aluminosilicate glasses.[31,32]

Using the half-step method, the Sn redox state was quantified from 1300°C to 1610°C (Figure 6B). As expected, an increase in temperature leads to a reduction of Sn, from 0% reduced at 1300°C to 25% reduced at 1610°C. However, the measurement at 1500°C deviates from this trend due to SnO_2 crystallization. These crystals dissolve into the glass when the temperature is increased to 1550°C. The temperature range over which SnO_2 crystallizes increases with the addition of Sn in the glass. For NASS0_20, SnO_2 crystallization occurs between 1450°C and 1550°C, thereby limiting the number of obtainable data points.

Using the in situ measurements displayed in Figure 6, the thermodynamics of Sn reduction can be modeled. By considering the reduction reaction shown in Equation (4), the redox state can be directly related to thermodynamic parameters:

$$-\frac{\Delta_r H_0}{RT}+\frac{\Delta_r S_0}{R}=\ln\left(\frac{\left[\mathrm{SnO}_4^{6-}\right]}{\left[\mathrm{SnO}_6^{8-}\right]}\right)+\ln\left(a_{\mathrm{O}^{2-}}\right)+\frac{2}{4}\ln\left(f_{\mathrm{O}_2}\right)+\ln\left(\frac{\gamma_{\mathrm{SnO}_4^{6-}}}{\gamma_{\mathrm{SnO}_6^{8-}}}\right) \tag{5}$$

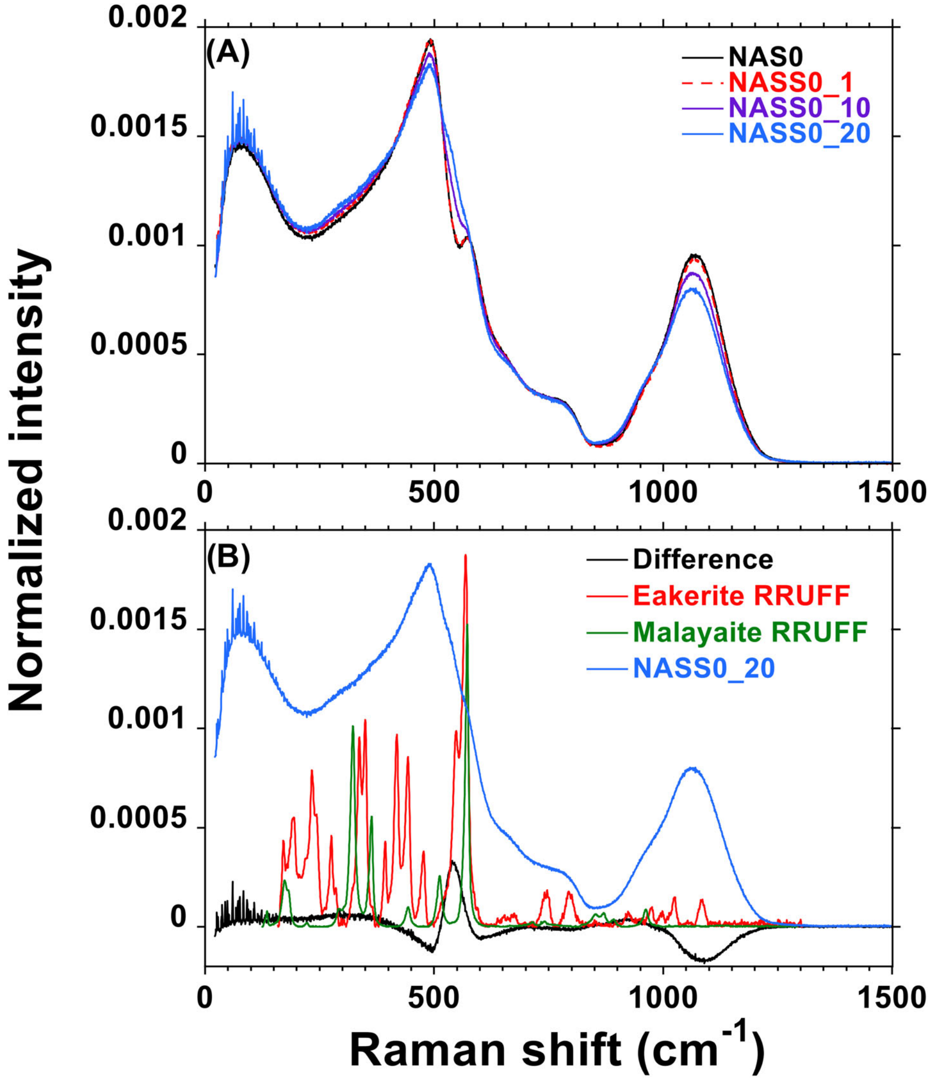

FIGURE 5 (A) Raman spectra of NAS0 glass and Sn-doped glasses. (B) Difference between the Raman spectra of NAS0 and NASS0_20. Eakerite and Malayaite reference spectra from the RUFF Raman database are given for comparison (R060319 and R061106). All glass spectra are normalized to the total area.

with $\Delta_r H_0$ the standard reduction enthalpy (J·mol^{-1}), $\Delta_r S_0$ the standard reduction entropy (J·mol^{-1}·K^{-1}), R the ideal gas constant (8.314 J·mol^{-1}·K^{-1}), and T the temperature in K. For a more detailed derivation of Equation (5) from Equation (4), readers are referred to a previous work.[54] Equation (5) can be rearranged by grouping terms that, to a first approximation, are independent of temperature under the denomination C:

$$\log\left(\frac{\left[\mathrm{SnO_4^{6-}}\right]}{\left[\mathrm{SnO_6^{8-}}\right]}\right) = -\frac{\Delta_r H_0}{2.303 * RT} + C - \frac{1}{2}\log\left(f_{O_2}\right) \quad (6)$$

C is a function of glass composition, oxygen fugacity, and total Sn concentration. As the parameter investigated here is temperature, C can be considered constant. Notably, C has the same dimensions as entropy and is sometimes named the apparent entropy. As all experiments were performed under air, the oxygen fugacity is set at 0.21. The slope of the $\log(f_{O_2})$ term is dependent on the number of electrons exchanged. In the case of Sn(II)/Sn(IV), the slope is ½. It will be ¼ for Ce(III)/Ce(IV), for instance. This means that the redox state of Sn is more sensitive to changes in oxygen fugacity than the redox state of Fe and Ce. Equation (6) shows a linear relationship between the log of the redox ratio and the reciprocal of temperature. Figure 7 illustrates these linear fits, not only for Sn but also for Ce and Fe.

The Sn redox ratio follows a linear relationship with the reciprocal temperature within the investigated range, which confirms that the redox states were measured at equilibrium. It is important to note that these linear fits

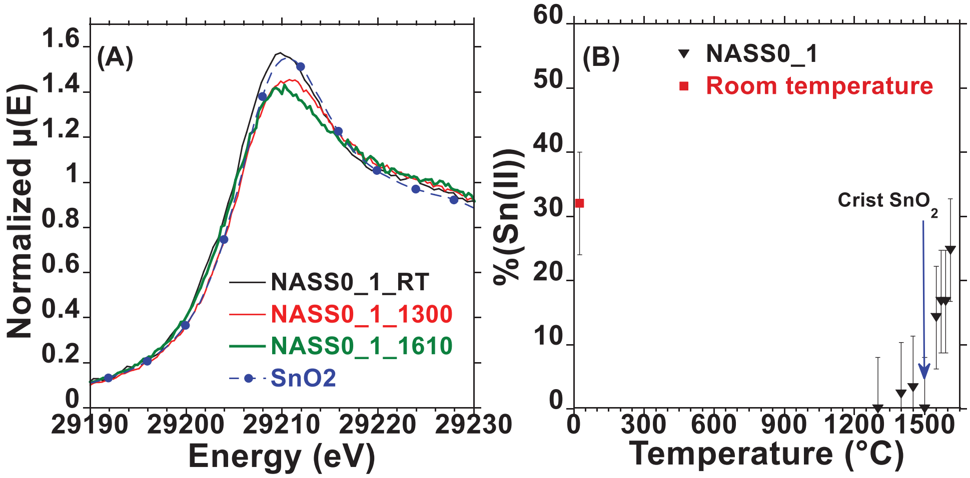

FIGURE 6 (A) Sn K-edge XANES (extended x-ray absorption fine structure) spectra of NASS0_1 sample equilibrated at different temperatures. Room temperature SnO_2 spectrum is given as a reference. (B) Evolution of the redox state of Sn in NASS0_1 at different temperatures determined by the half-step method.

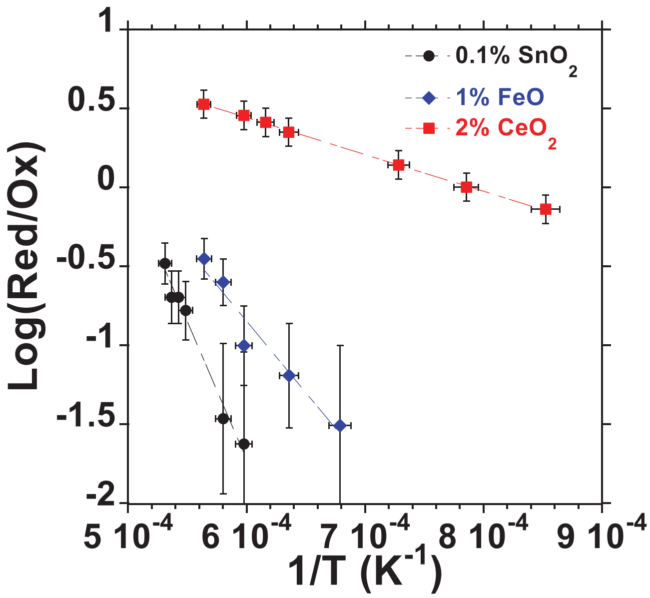

FIGURE 7 Equilibrium redox state in NAS as a function of reciprocal temperature (in K^{-1}) for Ce(III)/Ce(IV) (red squares),[32] Fe(II)/Fe(III) (blue diamonds),[31] and Sn(II)/Sn(IV) (black circles) (this study). Data points corresponding to temperatures where crystallization occurred were removed. The lines are linear regressions. Molar concentrations in multivalent elements are given in the labels.

are only valid under air in NAS glass and for a given concentration of the multivalent element. Similar trends have been reported for various elements in several glass compositions.[55–57] The electrochemical series obtained here is the following in terms of oxidizing power:

$$\mathrm{Sn\,(II)\,/Sn\,(IV)} < \mathrm{Fe\,(II)\,/Fe\,(III)} < \mathrm{Ce\,(III)\,/Ce\,(IV)}$$

This trend has been confirmed through studies on the mutual interactions between these three elements in silicate glass.[31,58,59] The reduction enthalpy can be calculated from the slope of the linear regression. In the case of Sn(II)/Sn(IV), we find a reduction enthalpy of 326 ± 25 kJ·mol^{-1}. This value is higher than those reported in the literature. In a sodium disilicate melt, Johnston[56] reports an apparent reduction enthalpy of 41 kJ·mol^{-1}, while Rüssel and Von der Gonna[55] report a value of 175 kJ mol^{-1}. These two studies indicate notably different results, even though they are both investigating the same composition. It is therefore not surprising that our value differs as we study an aluminosilicate melt. Despite these absolute differences, the relative reduction enthalpies of Sn(II)/Sn(IV), Fe(II)/Fe(III), and Ce(III)/Ce(IV) are consistent with the trend reported by Johnston:

$$\frac{\Delta_r H_{\mathrm{Ce}}\,(\text{Johnston})}{\Delta_r H_{\mathrm{Fe}}\,(\text{Johnston})} = 0.27 \qquad \frac{\Delta_r H_{\mathrm{Ce}}\,(\text{NAS})}{\Delta_r H_{\mathrm{Fe}}\,(\text{NAS})} = 0.26$$

$$\frac{\Delta_r H_{\mathrm{Ce}}\,(\text{Johnston})}{\Delta_r H_{\mathrm{Sn}}\,(\text{Johnston})} = 0.18 \qquad \frac{\Delta_r H_{\mathrm{Ce}}\,(\text{NAS})}{\Delta_r H_{\mathrm{Sn}}\,(\text{NAS})} = 0.14$$

The difference observed in the ratios of $\Delta_r H_{\mathrm{Ce}}$ to $\Delta_r H_{\mathrm{Sn}}$ between our study and the one by Johnston could be explained by the difference in concentration of multivalent elements. Indeed, Ce was introduced at 2 mol% while Sn was only present at 0.1 mol%. Our results agree with the electrochemical series reported in the literature. This shows that Sn, Ce, and Fe follow a similar behavior in peralkaline aluminosilicate melts as in sodium disilicate. However, this may not hold true for Sn in peraluminous compositions.[39]

Our findings not only confirm existing results but also show that thermodynamic parameters can be obtained

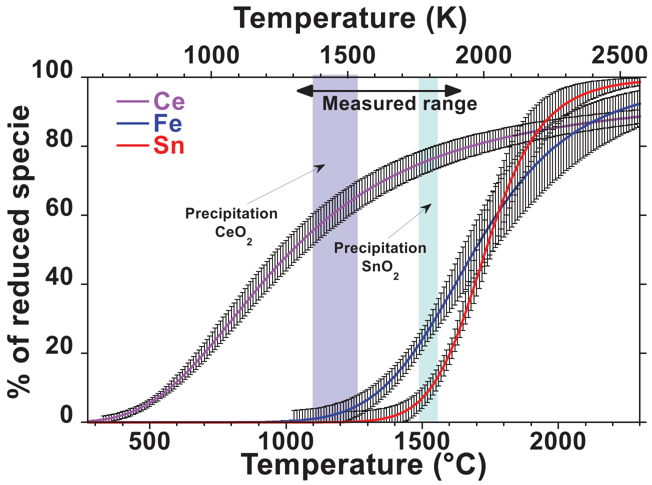

FIGURE 8 Modeled evolution of the reduced fractions at equilibrium for Ce, Fe, and Sn in NAS glass. The measured temperature range is highlighted in the figure, as well as the ranges of crystallization of CeO_2 and SnO_2 for the concentrations considered (see text for details). The relative error is calculated from the uncertainty in the linear fitting.

using in situ XANES spectroscopy. This is, to our knowledge, the first in situ direct comparison of Fe, Ce, and Sn behavior in an aluminosilicate composition.

4.4 | Comparison of Sn behavior with Ce and Fe: Application to fining

Although Figure 7 is a common representation of multivalent element behavior in glasses, it does not provide a straightforward way to determine the fraction of reduced species at a given temperature. Using the coefficients obtained from the linear fits, the percentage of reduced species can be predicted as a function of temperature (in K) for Ce, Fe, and Sn:

$$\%\mathrm{Ce\,(III)} = 100 * \frac{10^{\left(\frac{-2336}{T}+1.8\right)}}{1+10^{\left(\frac{-2336}{T}+1.8\right)}} \tag{7}$$

$$\%\mathrm{Sn\,(II)} = 100 * \frac{10^{\left(\frac{-17\,062}{T}+8.5\right)}}{1+10^{\left(\frac{-17062}{T}+8.5\right)}} \tag{8}$$

$$\%\mathrm{Fe\,(II)} = 100 * \frac{10^{\left(\frac{-9047}{T}+4.6\right)}}{1+10^{\left(\frac{-9047}{T}+4.6\right)}} \tag{9}$$

Using these three equations, it is possible to construct Figure 8 that compares the behavior of the three elements in NAS glass.

For the three elements studied, an increase in temperature leads to a reduction. However, the extent to which an element is reduced and the minimum temperature at which reduction is detected vary for each element. When the temperature is increased, Ce is the first element to be reduced, followed by Fe and then Sn. Notably, this order changes at higher temperatures, around 1750°C for Fe and Sn, if we extrapolate the model. This is due to the differing slopes of the Fe and Sn redox ratios in Figure 7. This difference in slopes can be traced back to the Sn(II)/Sn(IV) redox couple involving a two-electron exchange and having a higher reduction enthalpy than the Fe(II)/Fe(III) couple. It is interesting to note that Ce converges very slowly toward its fully reduced state. This behavior results not only from Ce having the lowest enthalpy of reduction among the three elements but also from the mathematical formulas of Equations (7)–(9). The redox curves are sigmoid with respect to $1/T$ and not T. This means that increasing the temperature becomes less effective to reduce a multivalent element beyond a certain temperature. Our measurements show that in our system, CeO_2 precipitates when the temperature is between 1100°C and 1250°C.[32] Similarly, SnO_2 precipitation has been evidenced in Figure 6B. It is therefore more correct to consider Ce and Sn redox states to be fully oxidized in their respective precipitation range, as they will form CeO_2 and $SnO_{2,}$ respectively.

It is also important to note that Equations (7)–(9) are given for a molar concentration of 2% for CeO_2, 1% for FeO, and 0.1% for SnO_2. Previous investigations have shown that the redox behavior of Ce is independent of its concentration over the 0.2–2 mol% concentration range.[32] Therefore, the Ce redox state model shown in Figure 8 can be applied for different concentrations. The same cannot be said for $SnO_{2,}$ as its redox state is very sensitive to its concentration (as discussed in Section 4.1).

The fining process is driven by gas release upon heating of the silicate melt.[17,19] As temperature increases, multivalent elements such as Ce and Sn are reduced. According to Equation (4), Sn reduction is responsible for the release of oxygen gas. These oxygen bubbles then coalesce with already existing bubbles (from air trapped in the raw materials or CO_2 from carbonates).[17] Larger bubbles are more easily able to escape the viscous silicate melt, which leads to the making of a final glass product without any bubbles.[60–62] This process is often referred to as the "primary fining step." However, some small residual bubbles may remain even after the reduction of fining agents such as CeO_2 or SnO_2. In such cases, a "secondary fining step" may be necessary to ensure the complete removal of residual bubbles in the final product. During this secondary step, the temperature is slightly decreased, by 50°C–100°C, which shifts the redox equilibria toward more oxidized states. As shown in Equation (4), an oxidation of Sn requires gaseous oxygen to occur. Therefore, the small residual bubbles will dissolve into the melt during the oxidation, completing the fining process.[18] Given the nature of the fining process, several criteria must be met for an oxide to be a suitable fining agent:

- The oxide must be the oxidized state of a multivalent couple (i.e., Ce(III)/Ce(IV)).
- The multivalent element must be partly reduced at the primary fining temperature (Tf_1).
- The multivalent element must be significantly more oxidized during the secondary fining (Tf_2) than during the primary fining.

Here, only fining with multivalent oxides is considered, excluding the addition of sulfates or nitrates. The main consideration to determine if an oxide is a suitable fining agent for a given glass composition is the glass viscosity. If the glass is too viscous during the oxygen bubble release, bubbles will be unable to escape the melt and will accumulate. This will lead to the formation of an insulating layer, made of gas bubbles, on top of the glass melt, which greatly reduces the furnace efficiency. This phenomenon is known as foaming and must be avoided.[18,63]

The viscosity curve of the undoped NAS0 glass can be found in Figure S2. Previous studies have shown that the addition of multivalent elements can modify the viscosity of glasses, but their influence is less pronounced at higher temperatures compared to near the glass transition temperature. This has been shown not only for Ce[48] but also for Fe.[6,64] Considering the relatively low amount of multivalent element considered here, the viscosities of Ce- and Fe-bearing NAS glass are unlikely to differ from that of NAS0 glass, especially at the highest temperatures required for fining (>1300°C). To our knowledge, no studies have been published on the effect of SnO_2 addition on the viscosity of silicate glasses. However, given the 0.1 mol% doping of SnO_2 considered in the present study, the viscosities of NAS0 and NASS0_1 are unlikely to differ substantially.

Figure 9 represents the redox equilibria as a function of viscosity. Redox equilibria are calculated from the previous equations and viscosity using the TVF equation given in Figure S2.

As illustrated in Figure 8, CeO_2 dissolves in NAS glass at about 1250°C, which corresponds to the superior limit of the precipitation range. Therefore, it is more correct to consider Ce to be fully oxidized until this temperature is reached. Once CeO_2 starts dissolving, the Ce redox state changes drastically, shifting from fully oxidized to 64% reduced at 1250°C. A simple reaction for CeO_2 dissolution and reduction can be written as:

$$CeO_{2(cryst)} \rightleftharpoons \frac{1}{2}Ce_2O_{3(melt)} + \frac{1}{4}O_{2(g)} \tag{10}$$

For each mole of CeO_2 reduced, a quarter of a mole of gaseous oxygen is produced. Given the predicted redox state for Ce at 1250°C, the amount of gaseous oxygen released is $0.64 \times 0.25 \times [Ce]_{tot}$ in moles. In NAS melt, this significant oxygen release occurs at a viscosity around $10^{3.04}$ Pa·s, which is too high for bubbles to escape the melt. One can estimate the time required for an oxygen bubble to travel 10 cm in a melt with this viscosity. This estimation has been done by Jackson et al.[25] using the Hadamard–Rybczynski equation.[65,66]

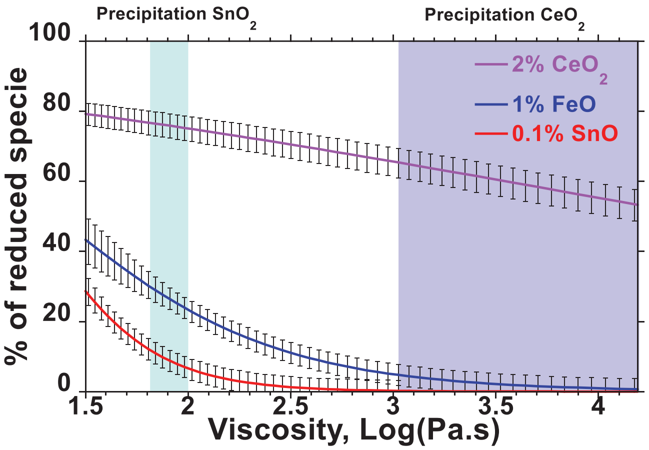

FIGURE 9 Modeled evolution of the reduced fractions at equilibrium for Ce, Fe, and Sn in NAS glass. The viscosity range presented is the one measured in Figure S2. Relative error is calculated from the uncertainty in the linear fitting of the redox state. The purple and cyan regions are taken from Figure 7.

$$u_\infty = \frac{R^2 g\,(\rho_b - \rho)}{3\eta} \tag{11}$$

with u_∞ the terminal velocity of the bubble, R the radius of the bubble, g the acceleration of gravity, ρ_b the density of the bubble, ρ the density of the melt, and η the viscosity. The difference between the bubble and the melt densities is considered to be independent of temperature and equal to 2520 kg·m^{-3}, as the density of NAS20 glass is 2521 kg·m^{-3} at room temperature.[32] Although the density of the melt is lower than that of the glass,[25] the difference is too small to impact the order of magnitude of the rise time. It is also important to note that the bubble radius can change during its ascent, typically decreasing.[60,62] This effect will not be taken into account here, as Jackson et al.[25] showed that fixing the bubble radius yields similar results to the fully integrated solution. For bubbles with radii of 0.5, 1, and 2 mm, the terminal velocities are $u_\infty = 1.9 \times 10^{-6}$, 7.5×10^{-6}, and 3.0×10^{-5} m·s^{-1}, respectively. These values imply that the fastest bubble (r = 2 mm) will take approximately 3300 s to rise 10 cm in NAS melt at 1250°C. The smallest bubble (r = 0.5 mm) will take 53 000 s (or ~15 h) to travel the same distance. Thus, the viscosity of NAS is too high at 1250°C to allow the bubbles to escape the melt. This will lead to foaming of the glass, which can be problematic during sample synthesis, as mentioned in a previous study.[32] Therefore, we can conclude that CeO_2 is not a suitable fining agent for NAS glass.

As illustrated in Figure 8, SnO_2 dissolves in NAS glass at about 1550°C. Therefore, it is more correct to consider Sn to be fully oxidized until this temperature is reached. Once SnO_2 starts dissolving, Sn redox state changes slightly, becoming 12% reduced at 1550°C. The reduction reaction follows the one presented in Equation (4). For each mole of SnO_2 reduced, half a mole of gaseous oxygen is produced. Given the predicted redox state for Sn at 1550°C, the amount of gaseous oxygen released is $0.12 \times 0.50 \times [\mathrm{Sn}]_{\mathrm{tot}}$ in moles. As Sn gains two electrons during its reduction, it releases twice as much oxygen per mole reduced compared to Ce. Comparing the theoretical amounts of oxygen release upon dissolution of CeO_2 and SnO_2 crystals at their respective dissolution temperatures, CeO_2 at 1250°C will release 0.16 moles of oxygen per mole of CeO_2, while SnO_2 at 1550°C will release 0.06 moles of oxygen per mole of SnO_2. Therefore, CeO_2 releases more oxygen than SnO_2 upon dissolution. However, the oxygen release from SnO_2 occurs at a viscosity of about 76 Pa·s (Figure 9). At this viscosity, bubbles with radii of 0.5, 1, and 2 mm will rise 10 cm in 3700, 900, and 230 s, respectively. Similar calculations were performed by Jackson et al.[25] when studying fining with Sb_2O_3. They determined the temperatures at which various bubble sizes escape the melt during a temperature increase and used these findings to assess the fining temperature.

All samples in our study were synthesized at 1600°C with an approximate viscosity of 42 Pa·s, which can be considered as Tf_1 for the primary fining step. At this temperature, the Sn redox state is 21% reduced, and the viscosity is low enough to allow for the removal of bubbles. For the secondary fining step, if we assume a temperature decrease of 50°C to 1550°C, the Sn redox change will shift from 21% reduced to 12% reduced, meaning a total of $0.09 \times 0.5 \times [\mathrm{Sn}]_{\mathrm{tot}}$ moles of oxygen being reabsorbed. If CeO_2 is considered as the fining agent, the Ce redox state at 1600°C is 80% reduced, while it is 78% reduced at 1550°C. This means that the amount of gaseous oxygen absorbed by Ce during the secondary fining is only $0.02 \times 0.25 \times [\mathrm{Ce}]_{\mathrm{tot}}$.

Based on these results, it appears that SnO_2 is better suited for fining NAS glass than CeO_2. For this reason, SnO_2 is used as a less toxic alternative to As_2O_5 and Sb_2O_5 as fining agents, particularly in glass products processed at high temperatures, such as LCD screens.[2,17,23,67] However, for a glass to be efficiently fined by SnO_2, the fining temperature must exceed the dissolution temperature of SnO_2 (i.e., higher than 1550°C). This is not the case for window glass compositions, which are usually processed at temperatures below 1300°C. Under such temperature conditions (and under air), Sn will be fully oxidized and, therefore, will not act as a fining agent (Figure 6B). The main limitation of using SnO_2 as a fining agent lies in the low solubility of Sn(IV).[67] As the in situ measurements suggest (Figure 6B), SnO_2 precipitates even when its concentration is only 0.1 mol%, significantly limiting the amount of SnO_2 that can be introduced in the raw materials and, therefore, the gaseous oxygen output.

On the other end, CeO_2 is not suited to fine viscous aluminosilicate melt as it releases oxygen at too low temperatures. Besides the discussion on the bubble dwell times, the existence of bubbles at low temperatures adds complexity to the industrial melting process.[68] There might be some upsides to having bubble release at lower temperatures. Even though the mobility of those bubbles is really low around 1300°C, this mobility will increase when they reach hotspots in the furnace. Those mobile "preexisting" bubbles near hotspots can have an impact similar to that of bubblers, improving recirculation motions within the melt.[20] It is important to note that this potential increase in convection is not possible if there are enough bubbles to induce foaming.

However, CeO_2 has been successfully used as a fining agent for silicate and borosilicate glasses processed at lower temperatures.[69] Additionally, CeO_2 has the advantage of oxidizing iron impurities coming from the raw materials, helping to decolorize the glass.[24,31] As shown in Figure 9, Fe_2O_3 undergoes reduction with temperature, contributing to the release of oxygen. This means that, in theory, Fe_2O_3 can be used as a fining agent. However, in practice, the presence of iron imparts color to the glass, which prohibits its use as a fining agent.

5 | CONCLUSION

Using Raman and EXAFS spectroscopy at Sn K-edge, we confirmed that Sn(IV) is in octahedral coordination in aluminosilicate glasses. The SnO_6^{8-} octahedra are corner-linked to TO_4 tetrahedra. These results also suggest that Sn(II) is in a lower coordination compared to Sn(IV). Having access to the anionic polyhedra of Sn(II) and Sn(IV) allowed us to correctly assess the oxygen behavior during Sn reduction. Moreover, we found that the Sn redox state at room temperature is strongly dependent on the total Sn concentration, with Sn being more oxidized at higher concentrations. In situ XANES spectroscopy at the Sn K-edge allowed the measurement of Sn redox equilibria at various temperatures. Using these measurements, we estimated the thermodynamic parameters that facilitate the prediction of Sn redox behavior as a function of temperature in NAS glass.

This model was then compared to those obtained for Ce and Fe in previous studies, highlighting the differences in redox behavior between the three multivalent elements, particularly regarding the amount of oxygen gas released in the glass at a given temperature. Viscosity measurements were used to model the behavior of oxygen gas bubbles in NAS melt. We demonstrated that the oxygen released by CeO_2 will not allow bubbles to escape from the melt within reasonable times, while the oxygen released by SnO_2 facilitates the removal of bubbles from the melt.

These in situ measurements provide a deeper understanding of the behavior of different multivalent oxides used as fining agents. Specifically, our findings explain why SnO_2 is a suitable fining agent for viscous aluminosilicate melts, offering a less toxic alternative to traditional fining agents such as As_2O_5 and Sb_2O_5.

AUTHOR CONTRIBUTIONS

Adrien Donatini: investigation (lead); visualization (lead); writing/original draft preparation (lead); writing/review and editing (equal). **Peggy Georges**: funding acquisition (lead); conceptualization (equal); resources (equal); supervision (equal); writing/review and editing (equal). **Tiphaine Fevre**: conceptualization (equal); supervision (equal); writing/review and editing (equal). **Laurent Cormier**: conceptualization (equal); resources (equal); supervision (equal); writing/review and editing (equal). **Daniel R. Neuville**: conceptualization (equal); resources (equal); supervision (equal); writing/review and editing (equal).

ACKNOWLEDGMENTS

The author has nothing to report.

CONFLICT OF INTEREST STATEMENT

The authors declare no conflicts of interest.

DATA AVAILABILITY STATEMENT

The data that support the findings of this study are available from the corresponding author upon reasonable request.

ORCID

Adrien Donatini https://orcid.org/0000-0002-8187-2470
Daniel R. Neuville https://orcid.org/0000-0002-8487-5001

REFERENCES

1. Onbaşlı MC, Tandia A, Mauro JC. Mechanical and compositional design of high-strength corning gorilla glass. In: Andreoni W, Yip S, editors. Handbook of materials modeling: applications: current and emerging materials. Cham: Springer International Publishing; 2018. p. 1–23. https://doi.org/10.1007/978-3-319-50257-1_100-1
2. Dejneka M, Kiczenski TJ. Display glass. In: Musgraves JD, Hu J, Calvez L, editors. Springer handbook of glass. Cham: Springer International Publishing: Cham; 2019. p. 1521–53. https://doi.org/10.1007/978-3-319-93728-1_45
3. Schaut RA, Peanasky JS, DeMartino SE, Schiefelbein SL. A new glass option for parenteral packaging. PDA J Pharm Sci Technol. 2014;68(5):527–34. https://doi.org/10.5731/pdajpst.2014.00998
4. Cormier L. Glasses: aluminosilicates. In: Pomeroy M, editor. Encyclopedia of materials: technical ceramics and glasses. Oxford: Elsevier; 2021. p. 496–518. https://doi.org/10.1016/B978-0-12-818542-1.00076-X
5. Lower NP, Brow RK, Kurkjian CR. Inert failure strains of sodium aluminosilicate glass fibers. J Non-Cryst Solids. 2004;344(1–2):17–21. https://doi.org/10.1016/j.jnoncrysol.2004.07.023
6. Chevrel MO, Giordano D, Potuzak M, Courtial P, Dingwell DB. Physical properties of $CaAl_2Si_2O_8$–$CaMgSi_2O_6$–FeO–Fe_2O_3 melts: analogues for extra-terrestrial basalt. Chem Geol. 2013;346:93–105. https://doi.org/10.1016/j.chemgeo.2012.09.004
7. Krstulović M, Rosa AD, Biedermann N, Irifune T, Wilke M. Structural changes in aluminosilicate glasses up to 164 GPa and the role of alkali, alkaline earth cations and alumina in the densification mechanism. Chem Geol. 2021;560:119980. https://doi.org/10.1016/j.chemgeo.2020.119980
8. Tanabe S, Hirao K, Soga N. Elastic properties and molar volume of rare-earth aluminosilicate glasses. J Am Ceram Soc. 1992;75(3):503–6. https://doi.org/10.1111/j.1151-2916.1992.tb07833.x
9. Makehima A, Tamura Y, Sakaino T. Elastic moduli and refractive indices of aluminosilicate glasses containing Y2O3, La2O3, and TiO2. J Am Ceram Soc. 1978;61(5–6):247–49. https://doi.org/10.1111/j.1151-2916.1978.tb09291.x
10. Tiegel M, Hosseinabadi R, Kuhn S, Herrmann A, Rüssel C. Young′s modulus, vickers hardness and indentation fracture toughness of alumino silicate glasses. Ceram Int. 2015;41(6):7267–75. https://doi.org/10.1016/j.ceramint.2015.01.144
11. Aaldenberg EM, Lezzi PJ, Seaman JH, Blanchet TA, Tomozawa M. Ion-exchanged lithium aluminosilicate glass: strength and dynamic fatigue. J Am Ceram Soc. 2016;99(8):2645–54. https://doi.org/10.1111/jace.14294
12. Nunes B, Pinho I, Cruz Fernandes J, Almeida RM, Santos LF. Mechanical properties of ion-exchanged alkali aluminosilicate glass. Int J Appl Glass Sci. 2023;14(1):155–64. https://doi.org/10.1111/ijag.16595
13. Comte M. Chapter 14: Commercial applications of glass-ceramics. In: From glass to crystal: Nucleation, growth and phase separation: from research to applications. EDP Sciences; 2017. p. 361–74. https://doi.org/10.1051/978-2-7598-1997-3.c021
14. Siebers F, Weiss E, Gabel F. Glass ceramic as a cooktop for induction heating having improved colored display capability and heat shielding, method for producing such a cooktop, and use of such a cooktop. US9018113B2; April 28, 2015. Accessed February 13, 2025. https://patents.google.com/patent/US9018113B2/en
15. Ross S, Welsch A-M, Behrens H. Lithium conductivity in glasses of the Li_2O–Al_2O_3–SiO_2 system. Phys Chem Chem Phys. 2014;17(1):465–74. https://doi.org/10.1039/C4CP03609C
16. Kim D-S, Dutton BC, Hrma PR, Pilon L. Effect of furnace atmosphere on E-glass foaming. J Non-Cryst Solids. 2006;352(50):5287–95. https://doi.org/10.1016/j.jnoncrysol.2006.08.035

17. Kim K. Fining behavior in alkaline Earth aluminoborosilicate melts doped with As2O5 and SnO2. J Am Ceram Soc. 2013;96(3):781–86. https://doi.org/10.1111/jace.12188
18. Leonard House K, Mazumder P, M Peterson I, Lee Schiefelbein S. Method of increasing the effectiveness of a fining agent in a glass melt. USOO7584632B2; 2009.
19. Hujova M. Influence of fining agents on glass melting: a review, part 1. Ceramics—Silikaty. 2017;61(2):119–26. https://doi.org/10.13168/cs.2017.0006
20. Borneto S, Cravero C, Lamberti A, Marsano D. Simulation and modelling approach for bubblers effect into Molten glass tank. Int J Multiphase Flow. 2024;181:105025. https://doi.org/10.1016/j.ijmultiphaseflow.2024.105025
21. Matyas J, Hrma PR. Sulfate fining chemistry in oxidized and reduced soda-lime-silica glasses, PNNL-15175, 15020694. USA: PNNL; 2005. https://doi.org/10.2172/15020694
22. Jones LE, Luo S. Nitrate fining and emissions during glass manufacturing. In: Environmental issues and waste management technologies in the materials and nuclear industries XII. John Wiley & Sons Ltd; 2009. p. 255–64. https://doi.org/10.1002/9780470538371.ch24
23. He X, Shen X, Huang Q, Zhang J, He Y, Liu T, et al. Study on the structure, fining and properties of non-alkali aluminoborosilicate glasses containing SnO2. J Non-Cryst Solids. 2021;559:120670. https://doi.org/10.1016/j.jnoncrysol.2021.120670
24. Vargin VV, Osadchaya GA. Cerium dioxide as a fining agent and decolorizer for glass. Glass Ceram. 1960;17(2):78–82. https://doi.org/10.1007/BF00692388
25. Jackson LE, Wadsworth FB, Mitchell J, Rennie C, Llewellin EW, Hess K, et al. Bubble rise in molten glasses and silicate melts during heating and cooling cycles. J Am Ceram Soc. 2022;105(12):7238–53. https://doi.org/10.1111/jace.18680
26. Le Losq C, Moretti R, Oppenheimer C, Baudelet F, Neuville DR. In situ XANES study of the influence of varying temperature and oxygen fugacity on iron oxidation atate and coordination in a phonolitic melt. Contrib Mineral Petrol. 2020;175(7):64. https://doi.org/10.1007/s00410-020-01701-4
27. Cicconi MR, Le Losq C, Henderson GS, Neuville DR. The redox behavior of Rare Earth elements. In: Moretti R, Neuville DR, editors. Geophysical monograph series. Wiley; 2021. p. 381–98. https://doi.org/10.1002/9781119473206.ch19
28. Berry AJ, Shelley JMG, Foran GJ, O'Neill HSC, Scott DR. A furnace design for XANES spectroscopy of silicate melts under controlled oxygen fugacities and temperatures to 1773 K. J Synchrotron Rad. 2003;10(4):332–36. https://doi.org/10.1107/S0909049503007556
29. Moretti R. Polymerisation, basicity, oxidation state and their role in ionic modelling of silicate melts. Ann Geophysics. 2005;48(4–5):340–68. https://doi.org/10.4401/ag-3221
30. Pinet O, Hugon I, Mure S. Redox control of nuclear glass. Proc Mater Sci. 2014;7:124–30. https://doi.org/10.1016/j.mspro.2014.10.017
31. Donatini A, Georges P, Fevre T, Cormier L, Neuville DR. Charge transfer between Ce and Fe during cooling of an aluminosilicate melt: an in situ XANES investigation. Inorg Chem. 2025;64(7):3528–40. https://doi.org/10.1021/acs.inorgchem.4c05223
32. Donatini A, Georges P, Fevre T, Cormier L, Neuville DR. Investigating cerium redox changes between aluminosilicate glass and melt: a multispectroscopic approach. The J Chem Phys. 2024;160:124503.
33. Neuville DR, Hennet L, Florian P, De Ligny D. In situ high-temperature experiments. Rev Mineral Geochem. 2014;78(1):779–800. https://doi.org/10.2138/rmg.2013.78.19
34. Neuville DR, Mysen BO. Role of aluminium in the silicate network: in situ, high-temperature study of glasses and melts on the join SiO_2-$NaAlO_2$. Geochim Cosmochim Acta. 1996;60(10):1727–37.
35. Newville M. Larch: an analysis package for XAFS and related spectroscopies. J Phys Conf Ser. 2013;430:012007. https://doi.org/10.1088/1742-6596/430/1/012007
36. Wojdyr MF. A general-purpose peak fitting program. J Appl Cryst. 2010;43(5):1126–28. https://doi.org/10.1107/S0021889810030499
37. Kubik E, Siebert J, Mahan B, Creech J, Blanchard I, Agranier A, et al. Tracing Earth's volatile delivery with tin. J Geophys Res Solid Earth. 2021;126(10):e2021JB022026. https://doi.org/10.1029/2021JB022026
38. Bourdon B, Pili E. Thermodynamic determination of condensation behavior for the precursory elements of radioxenon following an underground nuclear explosion. J Environ Radioact. 2023;261:107125. https://doi.org/10.1016/j.jenvrad.2023.107125
39. Farges F, Linnen RL, Brown GE. Redox and speciation of tin in hydrous silicate glasses: a comparison with Nb, Ta, Mo and W. Can Mineral. 2006;44(3):795–810. https://doi.org/10.2113/gscanmin.44.3.795
40. Ferreira G, P., Ligny D, D., Lazzari O, Jean A, Cíntora-González O, Neuville DR. Photoreduction of iron by a synchrotron x-ray beam in low iron content soda-lime silicate glasses. Chem Geol. 2013;346:106–12. https://doi.org/10.1016/j.chemgeo.2012.10.029
41. Ryerson FJ. Oxide solution mechanisms in silicate melts: systematic variations in the activity coefficient of SiO2. Cosmochim Acta. 1985;49(3):637–49. https://doi.org/10.1016/0016-7037(85)90159-0
42. Farges F, Linnen RL, Brown GE. Redox and speciation of tin in hydrous silicate glasses: a comparison with Nb, Ta, Mo AND W. Can Mineral. 2006;44(3):795–810. https://doi.org/10.2113/gscanmin.44.3.795
43. Moretti R, Ottonello G. 8 Silicate melt thermochemistry and the redox state of magmas. In: Neuville DR, Henderson GS, Dingwell DB, editors. Geological melts. De Gruyter; 2022. p. 339–404. https://doi.org/10.1515/9781501510939-009
44. Uchida H, Downs RT, Thompson RM. Reinvestigation of eakerite, $Ca_2SnAl_2Si_6O_{18}(OH)_2 \cdot 2H_2O$: H-atom positions by single-crystal x-ray diffraction and correlation with Raman spectroscopic data. Acta Cryst E. 2007;63 2):i47–i49. https://doi.org/10.1107/S1600536807002000
45. Newville M. Fundamentals of XAFS. Rev Mineral Geochem. 2014;78(1):33–74. https://doi.org/10.2138/rmg.2014.78.2
46. McKeown DA, Buechele AC, Gan H, Pegg IL. Tin valence and local environments in silicate glasses as determined from x-ray absorption spectroscopy. J Non-Cryst Solids. 2008;354(27):3142–51. https://doi.org/10.1016/j.jnoncrysol.2008.01.019
47. Kossiakoff AA, Leavens PB. The crystal structure of Eakerite, a calcium-tin silicate. Am Mineral. 1976;61:956–62.
48. Donatini A, Pereira L, Dingwell DB, Hess K, Müller D, Cormier L, et al. Influence of cerium addition and redox state on silicate

structure and viscosity. J Am Ceram Soc. 2024;108:jace.20113. https://doi.org/10.1111/jace.20113

49. McMillan P. Structural studies of silicate glasses and melts-applications and limitations of Raman spectroscopy. Am Mineral. 1984;69:622–44.
50. Le Losq C, Neuville DR, Florian P, Henderson GS, Massiot D. The role of Al^{3+} on rheology and structural changes in sodium silicate and aluminosilicate glasses and melts. Geochim Cosmochim Acta. 2014;126:495–517. https://doi.org/10.1016/j.gca.2013.11.010
51. Groat LA, Kek S, Schmidt C, Krane HG, Nistor L, Tendeloo GV. A synchrotron radiation, HRTEM, x-ray powder diffraction, and Raman spectroscopic study of malayaite, CaSnSiO5. Am Mineral. 1996;81(5). https://doi.org/10.2138/am-1996-5-606
52. Nemausat R, Gervais C, Brouder C, Trcera N, Bordage A, Coelho-Diogo C, et al. Temperature dependence of x-ray absorption and nuclear magnetic resonance spectra: probing quantum vibrations of light elements in oxides. Phys Chem Chem Phys. 2017;19(8):6246–56. https://doi.org/10.1039/C6CP08393E
53. Ellison AJG, Hess PC, Naski GC. Cassiterite solubility in high-silica K_2O-Al_2O_3-SiO_2 liquids. J Am Ceram Soc. 1998; 81(12):3215–20. https://doi.org/10.1111/j.1151-2916.1998.tb02758.x
54. Pinet O, Phalippou J, Di Nardo C. Modeling the redox equilibrium of the Ce^{4+}/Ce^{3+} couple in silicate glass by voltammetry. J Non-Cryst Solids. 2006;352(50–51):5382–90. https://doi.org/10.1016/j.jnoncrysol.2006.08.034
55. Rüssel C, von der Gönna G. The electrochemical series of elements in the $Na_2O{\cdot}2SiO_2$ glass melt. JNCS. 1999;260:147–54. https://doi.org/10.1016/S0022-3093(99)00563-3
56. Johnston WD. Oxidation–reduction equilibria in molten $Na_2O{\cdot}2SiO_2$ glass. J Am Ceram Soc. 1965;48(4):184–90. https://doi.org/10.1111/j.1151-2916.1965.tb14709.x
57. Schreiber HD. An electrochemical series of redox couples in silicate melts: a review and applications to geochemistry. J Geophys Res Solid Earth. 1987;92(B9):9225–32. https://doi.org/10.1029/JB092iB09p09225
58. Singh A. Role of tin as a reducing agent in iron containing heat absorbing soda-magnesia-lime-silica glass. Bull Mater Sci. 2004;27(6):537–41. https://doi.org/10.1007/BF02707282
59. Hayashi Y, Matsumoto K, Kudo M. The diffusion mechanism of tin into glass governed by redox reactions during the float process. J Non-Cryst Solids. 2001;282(2):188–96. https://doi.org/10.1016/S0022-3093(01)00319-2
60. Pereira L, Kloužek J, Vernerová M, Laplace A, Pigeonneau F. Experimental and numerical investigations of an oxygen single-bubble shrinkage in a borosilicate glass-forming liquid doped with cerium oxide. J Am Ceram Soc. 2020;103(12):6736–45. https://doi.org/10.1111/jace.17398
61. Pereira L, Podda O, Fayard B, Laplace A, Pigeonneau F. Experimental study of bubble formation in a glass-forming liquid doped with cerium oxide. J Am Ceram Soc. 2020;103(4):2453–62. https://doi.org/10.1111/jace.16950
62. Pigeonneau F, Pereira L, Laplace A. Dynamics of rising bubble population undergoing mass transfer and coalescence in highly viscous liquid. Chem Eng J. 2023;455:140920. https://doi.org/10.1016/j.cej.2022.140920
63. Beerkens R, Laimböck P. Foaming of glass melts. In: Kieffer J, editor. Ceramic engineering and science proceedings. Hoboken, NJ, USA: John Wiley & Sons Inc.; 2008. p. 41–58.
64. Sukenaga S, Cicconi MR, Yamada H, Wakihara T, Ohara K, Shibata H, et al. Iron redox effect on the structure and viscosity of a sodium silicate glass and melt. J Chem Phys. 2024;161(24):244503. https://doi.org/10.1063/5.0243427
65. Hadamard JS. Mouvement permanent lent d'une sphère liquide et visqueuse dans un liquide visqueux. C R Acad Sci. 1911;152:1735–52.
66. Rybczynski W. Über die fortschreitende bewegung einer flüssigen kugel in einem zähen medium. Akademia Umiejętności; 1911. p. 6.
67. Bookbinder AW, Ellison AJG, Lineman DM. Method of Fining Glass. WO 2006/115997 A2. WIPO; 2006.
68. Marcial J, Chun J, Hrma P, Schweiger M. Effect of bubbles and silica dissolution on melter feed rheology during conversion to glass. Environ Sci Technol. 2014;48(20):12173–80. https://doi.org/10.1021/es5018625
69. Fu J, Zhao J, Li S, Zhang H, Shi S, Zhang J, et al. Influence of CeO_2 on the structure and properties of borosilicate glass: an investigation from the perspective besides the refining process. J Non-Cryst Solids. 2024;623:122690. https://doi.org/10.1016/j.jnoncrysol.2023.122690

SUPPORTING INFORMATION

Additional supporting information can be found online in the Supporting Information section at the end of this article.

How to cite this article: Donatini A, Georges P, Fevre T, Cormier L, Neuville DR. Redox behavior of tin in aluminosilicate melts: Implications for the fining process. Int J Appl Glass Sci. 2025;e70006. https://doi.org/10.1111/ijag.70006